Dielectric Polarization-Filtering Metasurface Doublet for Trifunctional Control of Full-Space Visible Light

Song Gao, Changyi Zhou, Wenwei Liu, Wenjing Yue,* Shuqi Chen, Sang-Shin Lee, Duk-Yong Choi,* and Yang Li*

Multilayered plasmonic metasurfaces have been previously shown to enable multifunctional control of full-space electromagnetic waves, which are of great importance to the development of compact optical systems. While this structural configuration is practical for acquiring metasurfaces working in microwave frequency, it will inevitably become lossy and highly challenging to fabricate when entering the visible band. Here, an efficient yet facile approach to address this issue by resorting to a dielectric metasurface doublet (DMD) based on two vertically integrated polarization-filtering meta-atoms (PFMs) is presented. The PFMs exhibit polarization-dependent high transmission and reflection, as well as independent and full 2π phase control characteristics, empowering the DMD to realize three distinct incidence-direction and polarization-triggered wavefront-shaping functionalities, including anomalous beam deflection, light focusing, vortex beam generation, and holographic image projection as it is investigated either numerically or experimentally. The presented DMD undoubtedly holds several salient features compared with the multilayered metallic metasurfaces in aspects of design complexity, efficiency, and fabrication. Furthermore, as dielectric meta-atoms with distinct polarization responses can be deployed to construct the DMD, it is anticipated that diverse full-space metasurfaces equipped with versatile functionalities can be demonstrated in the future, which will greatly advance the development of multifunctional meta-optics.

1. Introduction

As an important research branch in nanophotonics, optical metasurfaces have attracted tremendous attention over the past decade. By elaborately designing the meta-atoms constituting a metasurface, local light properties can be arbitrarily manipulated at the subwavelength scale, making possible the planarization of conventional optical components like lens, prism, waveplate, polarizer, and beam splitter, among others.[1–10] Additionally, the flexible design strategies further enable metasurface to realize multidimensional manipulation of optical waves on a monolayer platform.[11–13] For instance, by resorting to light polarization, wavelength, and angle of incidence, as well as distinct spatial multiplexing schemes, abundant versatile multifunctional metasurfaces realizing distinct functionalities have been reported.[14–21] Despite the great success that has been achieved so far, it is worth mentioning that a majority of the reported multifunctional metasurfaces are only valid in one operation space — either transmission or reflection space.

An optical device that can independently control light in both transmission and reflection spaces is of great importance for the construction of ultra-compact optical systems. This has been lately realized based on multilayered metasurfaces.[22–29] It was reported that four layers of metallic patches can cooperate to enable polarization-related transmission/reflection control, making possible the independent light wavefront control in full spaces through meticulous design.[22] Based on a similar principle, five-layered plasmonic

S. Gao, W. Yue, Y. Li
School of Information Science and Engineering
Shandong Provincial Key Laboratory of Network Based Intelligent Computing
University of Jinan
Jinan, Shandong 250022, P. R. China
E-mail: ise_yuewj@ujn.edu.cn; ise_liy@ujn.edu.cn

C. Zhou, S.-S. Lee
Department of Electronic Engineering
Kwangwoon University
Seoul 01897, South Korea

W. Liu, S. Chen
The Key Laboratory of Weak Light Nonlinear Photonics
Ministry of Education
Renewable Energy Conversion and Storage Center
School of Physics and TEDA Institute of Applied Physics
Nankai University
Tianjin 300071, P. R. China

D.-Y. Choi
Laser Physics Centre
Research School of Physics
Australian National University
Canberra, ACT 2601, Australia
E-mail: duk.choi@anu.edu.au

The ORCID identification number(s) for the author(s) of this article can be found under https://doi.org/10.1002/lpor.202100603

metasurfaces were demonstrated to yield three wavefront manipulations through simultaneous selection of the incidence direction and light polarization.[23,25,27] It is noted that the reported metasurfaces realizing multifunctional full-space light control were mostly demonstrated in the microwave band and were prepared using the printed circuit board technology. However, it is apparent that directly transferring the abovementioned structural configuration to the visible band will be inevitably inefficient considering the intrinsic absorption loss of metals. Moreover, the practical implementations of the meta-atoms with considerably small dimensions and different geometries in multiple layers would indubitably make the nanofabrication too onerous and costly, which should be seriously considered when it comes to practical applications. Therefore, a novel and facile metasurface architecture that allows multifunctional control of full-space visible light with high efficiency and relaxed design complexity is urgently needed. Monolayer dielectric metasurfaces have been proved to be capable of realizing high-efficiency manipulation of visible light.[30,31] It can be expected that the degree of freedom in light control can be further extended by exploiting multilayered dielectric metasurfaces,[32] among which bilayer metasurfaces or metasurface doublet have received a burgeoning amount of interest lately. To date, most of the reported bilayer dielectric metasurfaces were demonstrated for operation in the near-infrared region and much of the effort were mainly devoted to monochromatic aberration correction,[33–35] multiwavelength control,[36–38] and light path or polarization control,[39–42] among others.[43–45] However, their potential in full-space light control remains unexplored.

Here, we demonstrate that highly-efficient and multifunctional control of full-space visible light can be readily achieved through a dielectric metasurface doublet (DMD). The DMD is an assembly of two vertically stacked rectangular lattice unit cells, each consisting of a polarization-filtering meta-atom (PFM) made of hydrogenated amorphous silicon (a-Si:H). Systematic numerical simulations are carried out to investigate the properties of the PFM in terms of its polarization-dependent transmission and reflection responses, and the relevant results indicate that high transmission and reflection, along with the full 2π-phase control could be independently attained from a monolayer PFM. On this basis, unlike previous four- and five-layered metallic metasurfaces, three distinct light manipulation functionalities can be easily realized by the DMD via controlling the light incidence and polarization. As the proof of concept, two DMDs enabling anomalous beam deflections and holographic image projections are numerically examined and a multifunctional DMD realizing light focusing and vortex beam generations in transmission and reflection spaces are successfully designed, fabricated, and characterized to validate our claim. We anticipate the proposed approach can enrich the development of multifunctional meta-optics and also open a new avenue to miniaturizing optical systems.

2. Results and Discussion

The concept of realizing trifunctional light control in both transmission and reflection spaces is depicted in **Figure 1**a. For a lossless optical device, incident light is either transmitted or reflected, leaving two spaces for potential multiplexing of distinct functionalities. Moreover, the light incidence from backward and forward direction can also be adopted to add more functionalities. Note that without breaking the symmetry along the propagation direction, the device will exhibit strong reciprocal transmission behaviors for backward and forward incidences.[46] Therefore, through meticulous design, three different functionalities or information can be possibly encoded in a single device. Toward this end, an elemental PFM, which is a type of meta-atom for realizing simultaneous polarization filtering and entire 2π phase control, is first proposed. Previous studies have shown that the metasurface constituents, which are nanoposts made of silicon, can be considered as waveguides truncated on both sides and operate as low-quality-factor Fabry–Pérot resonators.[47] As such structure allows the excitation of multiple modes propagating along the longitudinal direction and bouncing back at the output facet, both high transmission and reflection could be made possible through constructive and destructive interferences between these modes by finely tuning its thickness, despite the fact that most current researches focus on its operation in transmission mode. Furthermore, it is well known the output light phase can be tailored by adjusting the nanopost size, lattice pitches, or the gap distance between adjacent nanoposts.

Given the abovementioned analysis, the PFM is designed as shown in Figure 1b. The PFM is designed to operate at a wavelength $\lambda = 690$ nm. It is made of a-Si:H with thickness of H = 320 nm and is arranged in a rectangular lattice unit cell with asymmetric pitches of $P_x = 300$ nm, and $P_y = 360$ nm. The a-Si:H meta-atom ($n \approx 4.077 + 0.005i$) is placed on a glass substrate and encapsulated by SU-8 with a refractive index of 1.56. The responses for meta-atoms with various lateral dimensions are numerically investigated for incident light with polarization along x- (E_x) and y-axes (E_y). Considering the available structure size that can be fabricated with high precision, the minimum size of the meta-atom is determined to be 70 nm. Here, the transmission and reflection responses are respectively allocated to E_x and E_y polarizations, which is different from previous bifunctional polarization-controlled metasurfaces that merely concentrate the responses in one space. The simulated transmission (T_{Ex}) and reflection efficiencies (R_{Ey}) with respect to different meta-atom width (W) and length (L) are shown in Figure 1c, while the corresponding phase responses (φ_{Ex} and φ_{Ey}) are depicted in Figure 1d. The results show that high transmission and reflection along with full 2π phase control can be accomplished using the PFM. Furthermore, in order to arbitrarily shape the wavefront of transmitted and reflected light, one needs to search for appropriate meta-atoms which can independently impart phase delay covering full 2π range for both E_x and E_y polarizations. To simultaneously attain the desired phases and high transmission/reflection, the total complex amplitude error, defined as $\epsilon = |e^{i\varphi_T} - T_{Ex}e^{i\varphi_{Ex}}|^2 + |e^{i\varphi_R} - R_{Ey}e^{i\varphi_{Ey}}|^2$, is used to determine which meta-atom meets the requirement. Here, φ_T and φ_R represent the desired phases for transmitted E_x polarization and reflected E_y polarization, respectively. For a pair of desired φ_T and φ_R, the optimal candidate is selected when the complex amplitude error reaches the minimum. The corresponding width and length of the selected meta-atoms that can independently impart phase control from $-\pi$ to π for E_x and E_y polarizations are depicted in Figure 1e. The corresponding transmission/reflection efficiencies and phases of
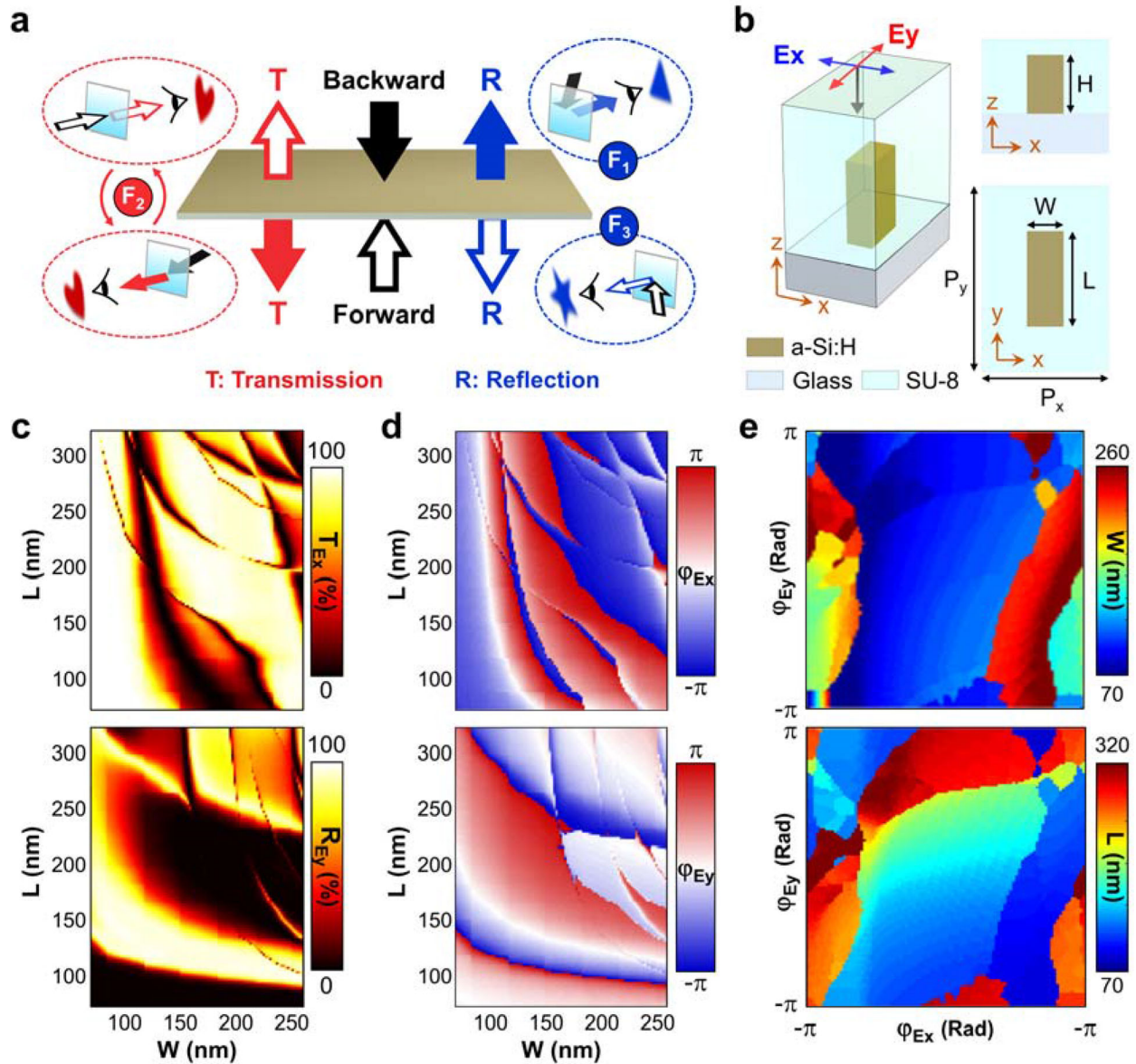
Figure 1. a) Concept of trifunctional light control in both transmission and reflection spaces upon backward and forward incidences. Three functions (denoted as F_1, F_2, and F_3) can be achieved. b) Schematic of the PFM unit cell. c) Simulated transmission and reflection c) efficiencies (T_{Ex}, R_{Ey}) and d) phases (φ_{Ex}, φ_{Ey}) for x- and y-polarizations, respectively, as a function of the meta-atom lateral dimensions (W, L) at designed wavelength of 690 nm. e) Selected values of W (top) and L (bottom) as functions of phases for x- (φ_{Ex}) and y-polarization (φ_{Ey}).

these meta-atoms are available in Figure S1 in the Supporting Information.

Unlike previously reported metasurfaces where control of the full-space light polarization and phase are separately realized by different layers, the proposed PFM can fulfill simultaneous manipulations of polarization and phase in a single layer. Therefore, by vertically integrating two such PFMs, three wavefront shaping functionalities can be possibly attained by changing the polarization state in two incidence directions. Subsequently, a DMD containing two PFM layers (MS1 and MS2) is constructed as schematically shown in **Figure 2**a. Anomalous beam deflections are first applied to check the feasibility of the DMD in enabling highly-efficient wavefront shaping of full-space visible

light. The MS1 contains eight distinct PFMs which form a supercell (Figure 2a) and are periodically arranged along the x- and y-directions. The same strategy is also applied to the construction of MS2 that is located beneath the MS1. To illustrate that the meta-atom in MS2 will not deteriorate the transmission response of the meta-atom in MS1, the transmission responses of the combined meta-atoms incorporating two layers of meta-atoms are further inspected. As shown in Figure S2 in the Supporting Information, by placing a selected PFM in the bottom layer while scanning the lateral dimension of the meta-atom in the top layer, the combined meta-atoms present nearly identical transmission responses to that in Figure 1c,d. According to the generalized Snell's law, the deflection angle of either transmitted
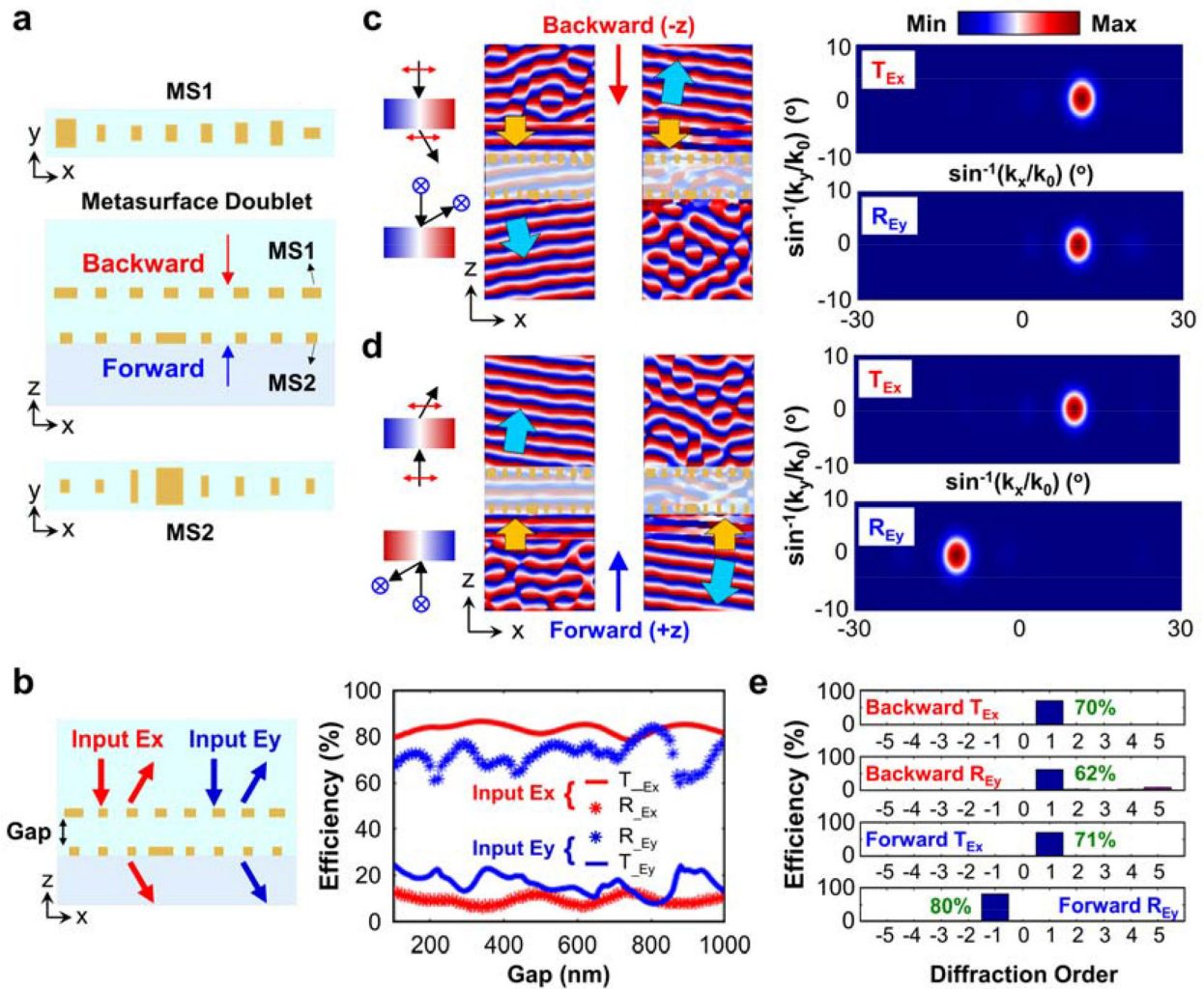
Figure 2. a) Schematic of the proposed metasurface doublet based on two layers of PFMs enabling anomalous transmission and reflection. b) Effect of the gap on the polarization-dependent total transmission and reflection efficiencies. Simulated phase wavefronts and far-field distributions of transmitted and reflected light upon c) backward, and d) forward incidence of E_x- and E_y-polarized light. e) Simulated polarization-dependent transmission and reflection efficiencies at various diffraction orders in backward and forward incidence cases. Numbers in the inset represent the anomalous beam deflection efficiencies at designed diffraction orders.

or reflected light can be predicted by taking account of the angle of incidence, refractive index of surrounding materials, and most importantly the local phase delay imparted by all meta-atoms in the metasurface. Here, the supercell of MS1 is designed to provide a linearly increasing phase delay from 0 to 1.75π along the x-axis for both E_x and E_y polarizations, whereas for the supercell of MS2, it imparts identical phase distribution for E_x polarization and a linearly decreasing phase delay from 1.75π to 0 for E_y polarization. Thus, for the E_x-polarized incident light, only MS1 provides a constant phase gradient which can lead to an anomalous beam transmission phenomenon. Additionally, the gap distance between the two layers should be examined to get an optimized structure configuration which can provide high transmission and reflection efficiencies. For the built DMD with various gap distances from 100 to 1000 nm, the simulated total transmission and reflection for polarization component identical to that of the incidence are plotted in Figure 2b. It can be seen that the E_x polariza-

tion component is mainly transmitted, while the E_y component is mainly reflected. We consider the gap distance of 800 nm as the optimal case since both transmission and reflection efficiencies can be higher than 80%, which is quite attractive for practical usage in visible band. Numerical simulations are further carried out to check the anomalous beam deflection phenomena. Upon backward normal incidence toward the −z direction, the phase wavefronts and far-field intensity profiles for transmitted and reflected light corresponding to the E_x and E_y incidence polarization components, respectively, are simulated as depicted in Figure 2c. It is found that the transmitted (reflected) light is redirected to an oblique angle of 11.21° (10.71°) through the anomalous deflection effect, which is quite close to the theoretical value of 11.39° (10.62°) corresponding to the +1st diffraction order. These performances for the forward incidence case (toward +z direction) are also presented in Figure 2d, where incident light is transmitted and reflected mainly toward 10.71° and −11.44°, respectively. The

**ADVANCED
SCIENCE NEWS**

www.advancedsciencenews.com

LASER
& PHOTONICS
REVIEWS

www.lpr-journal.org

unequal beam deflection angles for both transmitted and reflected light upon backward and forward incidences can be attributed to the slight refractive index differences between glass and SU-8. The transmission and reflection efficiencies upon backward and forward incidences at various diffraction orders are summarized in Figure 2e. Specifically, for backward incidence, efficiencies of transmitted E_x and reflected E_y polarizations at desired +1st diffraction order are estimated to be 70% and 62%, respectively. For forward incidence case, the transmitted E_x and reflected E_y polarization efficiencies at desired +1st and −1st diffraction orders are 71% and 80%, respectively. The average anomalous beam deflection efficiency of the abovementioned four cases is in the vicinity of 70%, denoting an excellent ability of the proposed DMD for full-space visible light manipulation.

Although there are some fluctuations in the anomalous beam deflection efficiencies, it can be inferred from Figure 2b that high anomalous beam deflection performances can be overall well-maintained at various gap distances. One should also be concerned about the misalignment effect when it comes to a design with multilayered configuration. For the proposed DMD, it can be understood that the function of reflected light is solely determined by one metasurface layer, thus only transmitted light can be possibly affected by the misalignment. Additional numerical simulations are performed to investigate the anomalous beam deflection performances under various misalignment situations for both E_x- and E_y-polarized incidences from backward and forward directions (Figure S3 in the Supporting Information). Here, the relative misalignment between the supercell MS1 and supercell MS2 is more specifically defined as the central position of each meta-atom in the top and corresponding bottom metasurface layers, and the misalignments along x- and y-axes are denoted as Δx and Δy, respectively. It can be found that all anomalous beam deflection performances can be well-preserved for Δx ranging from −150 to 150 nm and Δy from −180 to 180 nm (half of the lattice periods). These results guarantee that the proposed DMD has a nearly alignment-independent performance. In addition to the DMD enabling anomalous beam deflections, a multifunctional DMD, which can be seen as the integration of one transmissive focused vortex beam generator and two distinct off-axis parabolic mirrors, is also proposed and experimentally implemented. Based on the above analysis, we suggest to fabricate the multifunctional DMD via standard nanofabrication techniques including two-step lift-off processes, along with highly accurate overlay alignment in the electron beam lithography (EBL) process as schematically illustrated in **Figure 3**a.[48]

The proposed multifunctional DMD is designed to support three wavefront shaping functionalities. Upon backward incidence, the E_y-polarized plane wave will be reflected and focused to the SU-8 side (F_1), while the incident E_x polarization will be transmitted and transformed into a focused vortex beam (F_2). For the forward incidence case, the E_y polarization will be reflected and focused in the substrate side (F_3). The transmission behaviors of a traditional metasurface incorporating the proposed DMD are generally symmetric and thus the corresponding wavefront shaping functionalities hold the same for both backward and forward incident E_x polarizations. However, noting that there should be a slight difference (for instance, the focal position of the vortex beam) between the two cases since the refractive indices of glass and SU-8 are slightly different. The phase profiles for realizing the abovementioned three functionalities can be

described as

$$
\varphi_{F_m}(x,y)
$$

$$
= \begin{cases}
\frac{2\pi n_1}{\lambda}\left(f_m - \sqrt{(x-x_{Fm})^2 + (y-y_{Fm})^2 + f_m{}^2}\right), m=1 \\
\frac{2\pi n_{m\mp1}}{\lambda}\left(f_m - \sqrt{(x-x_{Fm})^2 + (y-y_{Fm})^2 + f_m{}^2}\right) + l\tan^{-1}\left(\frac{y}{x}\right), m=2 \\
\frac{2\pi n_3}{\lambda}\left(f_m - \sqrt{(x-x_{Fm})^2 + (y-y_{Fm})^2 + f_m{}^2}\right), m=3
\end{cases}
$$

$$(1)$$

where (x_{Fm}, y_{Fm}) and f_m ($m = 1, 2, 3$) represent the focal position and focal length of the function F_m, respectively, while l stands for the topological charge of the vortex beam. Besides, n_1 and n_3 stand for the refractive index of SU-8 and glass, respectively. The multifunctional DMD is designed to have a circular shape with 240×200 unit cells along x- and y-directions, respectively, corresponding to a diameter of 72 µm. The focal lengths f_1, f_2, f_3 are set to be 60, 80, and 156 µm, respectively, and the topological charge of the vortex beam is $l = 3$. The focal positions (x_{F1}, y_{F1}), (x_{F2}, y_{F2}), and (x_{F3}, y_{F3}) are chosen to be (−20, 0) µm, (0, 0) µm, (10, 0) µm, respectively. The calculated phase profiles and the geometries of corresponding top MS1 and bottom MS2 are shown in Figure 3b. We have also conducted numerical simulations to check the three functionalities, where only the central row is considered due to the limited computational resources. As shown in Figure S4 in the Supporting Information, all expected wavefront shaping functionalities have been confirmed. The optical and scanning electron microscope (SEM) images of the fabricated DMD including the bottom MS2 (taken before fabrication of MS1) and top MS1 are provided in Figure 3c.

The performances of the fabricated multifunctional DMD are subsequently characterized. The measured transmission and reflection field intensity profiles (xz-plane), representing the light beam trajectory, upon backward and forward incidences with E_x- and E_y-polarizations, are presented in Figure 4. For the backward incidence, the evolution of the intensity distributions reveals that incident E_y polarization gets reflected and focused at $z \approx -40$ µm plane, and the focal point is located at the position $(x_{F1}, y_{F1}) = (−19.7, 0)$ µm with a diameter of ≈ 2.6 µm. The incident plane wave of E_x polarization is transmitted and clearly transformed into a focused vortex beam featuring doughnut-shaped intensity distribution with a ring-diameter of ≈ 2.2 µm at $z \approx 60$ µm plane. For the forward incidence case, a focused vortex beam can be clearly witnessed in the transmission space at $z \approx 65$ µm for incidence E_x polarization, whereas the incident plane wave of E_y polarization is gradually focused at the position $(x_{F3}, y_{F3}) = (9.73, 0)$ µm in the reflection space and nearly 120 µm away from the sample surface. The mismatches between the simulated and measured focal planes are likely caused by the imperfection in measurement and the fabricated sample, for instance, the refractive index difference between SU-8 and the cover-slip. The quality of the focused vortex beam is found better in the backward incidence case than that of the forward incidence case, which might be caused by the impurity substances induced in the cover-slip and the misalignment between two layers. Nevertheless, as the designed three wavefront-shaping functionalities
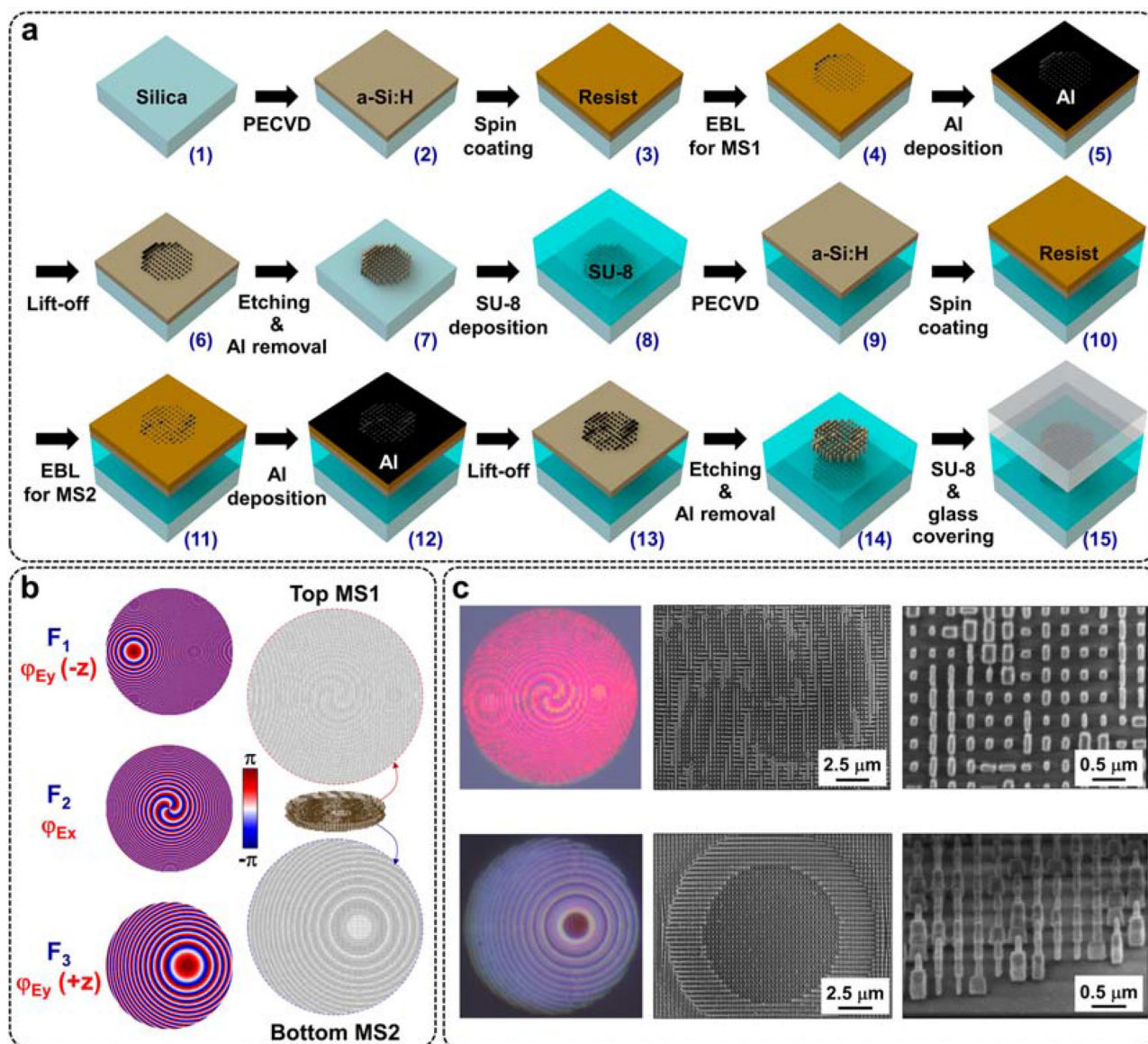
Figure 3. a) Flow chart illustrating the fabrication procedure of the proposed DMD. b) Calculated phase profiles for obtaining off-axis light focusing functionalities (F_1 and F_3) and vortex beam generation (F_2), and the geometries of the designed top MS1 and bottom MS2 constituting the proposed multifunctional DMD. c) Microscopy and SEM images of the MS1 and MS2 that are taken during fabrication of the DMD.

have been witnessed in expected transmission and reflection spaces, the effectiveness of our proposed approach can be ensured.

Based on the proposed approach, we also carry out numerical simulations to further demonstrate a DMD which can project three distinct holographic images in full spaces. **Figure 5** shows the target images (star, heart, triangle), their corresponding phase distributions derived from the Gerchberg–Saxton algorithm,[49] and the geometries of the top and bottom metasurface layers constituting the DMD, as well as the simulated far-field intensity profiles. Due to the limited computation resources, only 40 × 40 unit cells are incorporated into each metasurface layer, leading to the degraded image quality. Nevertheless, the results successfully indicate the presented method can find

promising applications in multidimensional information display and encryption.

3. Conclusion

In summary, a facile yet efficient DMD platform has been proposed and demonstrated to realize trifunctional manipulation of full-space visible light. It is shown that the polarization-dependent high transmission/reflection and independent full 2π phase control ability of the PFM constituting the DMD make possible the integration of three distinct functionalities on a single device through controlling the incidence direction and polarization. This claim has been numerically verified by a DMD en-
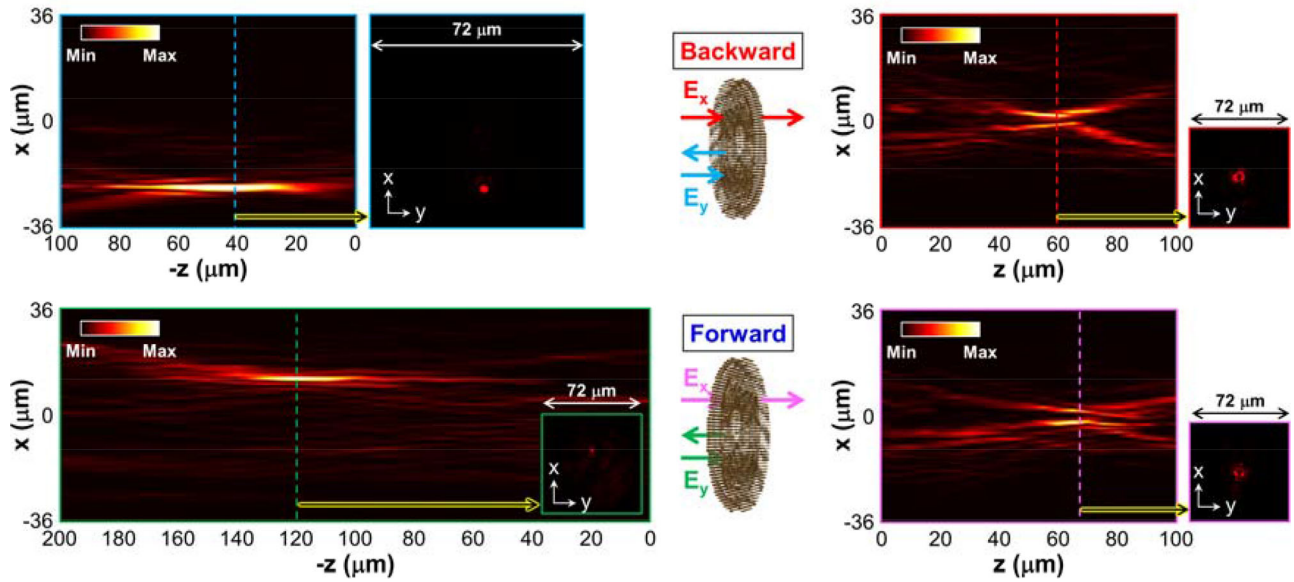
Figure 4. Measured field intensity profiles (xz-plane) for backward and forward incident light with E_x- and E_y-polarizations. Field intensity profiles (xy-plane) at the focal plane are also included.
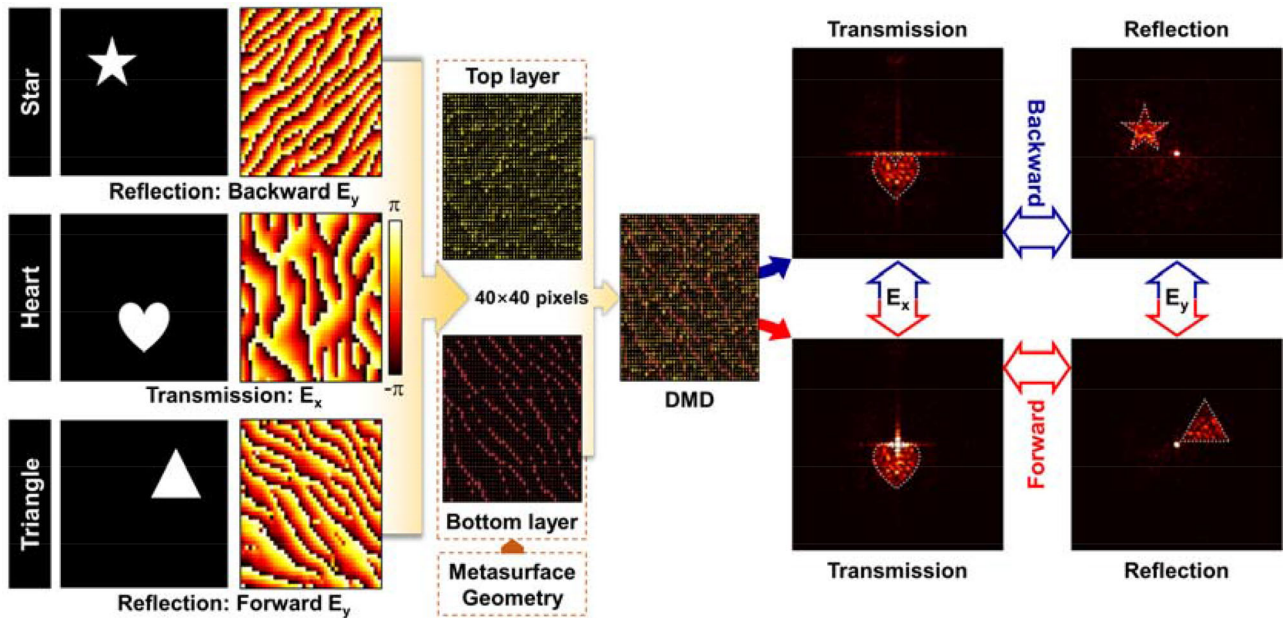

Figure 5. A DMD designed for projecting three distinct holographic images in full spaces.

abling full-space anomalous beam deflections with an average anomalous beam deflection efficiency of ≈70% at an operation wavelength of 690 nm, and experimentally validated through a DMD sample which realized light focusing and focused vortex beam generations. As such, we believe the proposed DMD outperforms previous multilayered metallic metasurfaces in terms of design complexity, efficiency, and fabrication and may find prominent applications in multidimensional full-space optical information processing. Additionally, we anticipate the presented method can give new inspirations to the design of multilayered dielectric metasurfaces since meta-atoms with different polariza-

tion responses can be utilized in the design, which we believe will greatly advance the development of multifunctional meta-optics in the future.

4. Experimental Section

Nanofabrication: The multifunctional DMD was prepared via standard nanofabrication techniques including double electron beam lithography (EBL) and Al etch mask liftoff, followed by silicon plasma etching; in addition, SU-8 interlayer was placed to separated two metasurfaces as

**ADVANCED
SCIENCE NEWS**

www.advancedsciencenews.com

LASER
& PHOTONICS
REVIEWS

www.lpr-journal.org

represented in Figure 3a. Hydrogenated amorphous silicon (a-Si:H) was deposited using plasma-enhanced chemical vapor deposition (Plasmalab 100 from Oxford) on SiO$_2$ substrate. Next, a positive electron beam resist (ZEP520A from Zeon Chemicals) of 300 nm was spin-coated on the film. Considering the performance of the DMD is nearly independent of the misalignment, MS2 and two alignment marks surrounding MS2 were written on the resist using EBL (Raith150) accompanied by a development in ZED-N50. The relative positions of MS2 with respect to the alignment marks can be known. Then, an aluminum film of 50 nm thickness was deposited via electron-beam evaporation (Temescal BJD-2000) on the substrate, and it was patterned by lifting off the resist using a solvent (ZDMAC from Zeon Co.). The patterned aluminum was utilized as a hard mask during dry etching, thereby transferring the designed pattern to the underlying a-Si:H layer through fluorine-based inductively-coupled-plasma reactive ion etching (Oxford Plasmalab System 100). The residual aluminum from the patterned nanopillars was etched in phosphoric/nitric/acetic acids mixed solution. Subsequently, a layer of SU-8 polymer with a proper thickness was spin-coated onto the sample and UV-cured. Note that both the thickness of the a-Si:H layer and the designed interlayer gap distance should be considered to determine the final thickness of SU-8 for spin coating ($\approx$1100 nm). As SU-8 is liquid, it can easily fill the gap between the structures during spin coating. The SU-8 polymer shows high transparency so that the two alignment marks can be clearly seen under the electron beam microscope. Subsequently, MS1 was constructed by carrying out a series of the same processes, including resist spin coating, EBL, aluminum deposition, lift-off, plasma etching, and aluminum removal. As a final step, $\approx$2 μm thick SU-8 was spin-coated; then, 200 μm thick cover-slip (with refractive index similar to SU-8) put in contact with it, and the polymer UV-cured. The alignment precision of the developed DMD is at a few micrometer-scale. In other cases when the misalignment severely affects the device's performance, one could consider using four alignment marks surrounding the metasurface to improve the alignment precision up to several tens nanometer. It is believed that the SU-8 layer encapsulating the MS2 would have a low surface roughness since the SU-8 liquid with much larger thickness than a-Si:H can fulfill the gap between nanostructures.[50,51]

Optical Characterization: For the characterization of the multifunctional DMD, a supercontinuum laser ("SuperK Compact," NKT Photonics) is used to emit an unpolarized broadband light, which then passes through a filter ("FB690-10", Thorlabs) and a linear polarizer ("LPNIR050-MP2," Thorlabs), and is then slightly focused onto the sample via a lens ("AC254," Thorlabs). The transmitted light intensity distribution in xy-plane is then imaged by a customized imaging system including an objective lens ("50×/0.4," Mitutoyo), a tube lens and a camera ("BU302MCF," Toshiba). The microscope imaging system is first adjusted to let the objective focus coincides with the DMD surface (defined as z = 0 μm). The imaging system is then moved along the positive z-axis in steps of 5 μm to record the intensity images at various distances away from the sample. The plotted xz-plane in Figure 4 of the main text are realized by extracting the intensity along the transverse line connecting the centers of all recorded intensity patterns (xy-plane). For characterizing the multifunctional DMD performances in reflection spaces, a cube beam splitter ("32 600," Edmund Optics) is placed between the lens and the sample. Meanwhile, the imaging system is rotated by 90° so as to record the reflected light intensity distribution (xy-plane). The trajectory of reflected beam in xz-plane as illustrated Figure 4 of the main text are also realized based on the same method as abovementioned. Schematics for the measurement setup and sample flipping can be found in Figure S5 in the Supporting Information.

Numerical Simulation: A finite-difference time-domain (FDTD) method-based tool named FDTD Solutions was used to simulate the optical performances of the PFM unit cell and various DMD designs. i) The transmission/reflection efficiencies and corresponding phase responses depicted in Figure 1c–e were calculated by scanning the lateral dimensions of the meta-atom (a-Si:H nanopost). The width and length were swept from 70 to 260 nm and from 70 to 320 nm, respectively, with identical scanning steps of 2 nm. Periodic boundary conditions were applied to the x- and y-boundaries, while perfectly matched layer (PML) boundary conditions were applied to the z-axis. A plane wave source with an operating wavelength of $\lambda = 690$ nm was embedded in the substrate side and positioned 1 μm below the meta-atom. A "2D Z-normal" power monitor and a point monitor are positioned 1 μm above (below) the meta-atom (light source) to record the transmission (reflection) efficiencies and phase responses, respectively. ii) For the simulation of the DMD enabling anomalous beam deflections shown in Figure 2c,d, two layered supercells containing 16 meta-atoms with designed lateral dimensions were constructed through a script. Boundary conditions for this case are identical to that of the simulation for the unit cell. A "2D Z-normal" power monitor and a "2D Y-normal" field profile monitor were used to record the far-field intensity distributions and the phase wavefronts (xz-plane), respectively. iii) For the simulation of the multifunctional DMD empowering light focusing and vortex beam generation shown in Figure S4 (Supporting Information), only the central row along the x-axis was considered. Each layer of the DMD consists of 240 meta-atoms with designed width and length, which was constructed through a script. The boundary conditions for this case along the y- and x-axes were set to be periodic and PML respectively. The computation region along the x-axis was 1 μm larger than the DMD. A total-field scattered field (TFSF) source was utilized to feed the DMD from the substrate (SU-8) side for the forward (backward) incidence case. iv) For the simulation of the DMD for projecting hologram images, PML boundary conditions were set along the x-, y-, and z-axes. Each layer of the DMD comprises 40 × 40 = 1600 meta-atoms corresponding to a lateral area of 12 × 14.4 μm². The computation region was set to be 14.5 and 17 μm along the x- and y-axes, respectively, and 2.6 μm along the z-axis. Again, the TFSF source was used to feed the DMD. The simulated light intensities as illustrated in Figure 5 were calculated by the "farfield3d" command using a script.

Supporting Information

Supporting Information is available from the Wiley Online Library or from the author.

Acknowledgements

Conflict of Interest

The authors declare no conflict of interest.

Data Availability Statement

The data that support the findings of this study are available from the corresponding author upon reasonable request.

Keywords

[1] M. Khorasaninejad, W. T. Chen, R. C. Devlin, J. Oh, A. Y. Zhu, F. Capasso, *Science* **2016**, *352*, 1190.

[2] M. Khorasaninejad, F. Capasso, *Science* **2017**, *358*, eaam8100.

[3] S. Wang, P. C. Wu, V.-C. Su, Y.-C. Lai, M.-K. Chen, H. Y. Kuo, B. H. Chen, Y. H. Chen, T.-T. Huang, J.-H. Wang, R.-M. Lin, C.-H. Kuan, T. Li, Z. Wang, S. Zhu, D. P. Tsai, *Nat. Nanotechnol.* **2018**, *13*, 227.

[4] G. Yoon, K. Kim, S.-U. Kim, S. Han, H. Lee, J. Rho, *ACS Nano* **2021**, *15*, 698.

[5] Z. Li, E. Palacios, S. Butun, K. Aydin, *Nano Lett.* **2015**, *15*, 1615.

[6] S. Gao, C.-S. Park, S.-S. Lee, D.-Y. Choi, *Nanoscale* **2019**, *11*, 4083.

[7] P. C. Wu, W. Y. Tsai, W. T. Chen, Y. W. Huang, T. Y. Chen, J. W. Chen, C. Y. Liao, C. H. Chu, G. Sun, D. P. Tsai, *Nano Lett.* **2016**, *17*, 445.

[8] F. Ding, Y. Chen, S. I. Bozhevolnyi, *Photonics Res.* **2020**, *8*, 707.

[9] F. Ding, R. Deshpande, C. Meng, S. I. Bozhevolnyi, *Nanoscale* **2020**, *12*, 14106.

[10] S. Gao, C. Zhou, W. Yue, Y. Li, C. Zhang, H. Kan, C. Li, S.-S. Lee, D.-Y. Choi, *ACS Appl. Mater. Interfaces* **2021**, *13*, 14497.

[11] Y. Hu, X. Wang, X. Luo, X. Ou, L. Li, Y. Chen, P. Yang, S. Wang, H. Duan, *Nanophotonics* **2020**, *9*, 3755.

[12] S. Chen, W. Liu, Z. Li, H. Cheng, J. Tian, *Adv. Mater.* **2020**, *32*, 1805913.

[13] Y. Zhang, H. Liu, H. Cheng, J. Tian, S. Chen, *Opto-Electron. Adv.* **2020**, *3*, 200002.

[14] S. Gao, C.-S. Park, C. Zhou, S.-S. Lee, D.-Y. Choi, *Adv. Opt. Mater.* **2019**, *7*, 1900883.

[15] Z. Shi, M. Khorasaninejad, Y.-W. Huang, C. Roques-Carmes, A. Y. Zhu, W. T. Chen, V. Sanjeev, Z.-W. Ding, M. Tamagnone, K. Chaudhary, R. C. Devlin, C.-W. Qiu, F. Capasso, *Nano Lett.* **2018**, *18*, 2420.

[16] S. M. Kamali, E. Arbabi, A. Arbabi, Y. Horie, M. S. Faraji-Dana, A. Faraon, *Phys. Rev. X* **2017**, *7*, 041056.

[17] Z. Shi, A. Y. Zhu, Z. Li, Y.-W. Huang, W. T. Chen, C.-W. Qiu, F. Capasso, *Sci. Adv.* **2020**, *6*, eaba3367.

[18] J. Jin, X. Li, M. Pu, Y. Guo, P. Gao, M. Xu, Z. Zhang, X. Luo, *iScience* **2021**, *24*, 102107.

[19] W. Yang, G. Qu, F. Lai, Y. Liu, Z. Ji, Y. Xu, Q. Song, J. Han, S. Xiao, *Adv. Mater.* **2021**, *33*, 2101258.

[20] X. Zhang, M. Pu, Y. Guo, J. Jin, X. Li, X. Ma, J. Luo, C. Wang, X. Luo, *Adv. Funct. Mater.* **2019**, *29*, 1809145.

[21] Y. Guo, S. Zhang, M. Pu, Q. He, J. Jin, M. Xu, Y. Zhang, P. Gao, X. Luo, *Light Sci. Appl.* **2021**, *10*, 63.

[22] T. Cai, G. Wang, S. W. Tang, H. X. Xu, J. W. Duan, H. J. Gao, F. X. Guan, S. L. Sun, Q. He, L. Zhou, *Phys. Rev. Appl.* **2017**, *8*, 034033.

[23] L. Zhang, R. Y. Wu, G. D. Bai, H. T. Wu, Q. Ma, X. Q. Chen, T. J. Cui, *Adv. Funct. Mater.* **2018**, *28*, 1802205.

[24] H. Yi, S.-W. Qu, K.-B. Ng, C. K. Wong, C. H. Chan, *IEEE Trans. Antennas Propag.* **2018**, *66*, 209.

[25] W. Pan, T. Cai, S. Tang, L. Zhou, J. Dong, *Opt. Express* **2018**, *26*, 17447.

[26] Y. Jing, Y. Li, J. Zhang, J. Wang, M. Feng, H. Ma, S. Qu, *Opt. Express* **2019**, *27*, 21520.

[27] R. Y. Wu, L. Zhang, L. Bao, L. W. Wu, Q. Ma, G. D. Bai, H. T. Wu, T. J. Cui, *Adv. Opt. Mater.* **2019**, *7*, 1801429.

[28] H. L. Wang, H. F. Ma, M. Chen, S. Sun, T. J. Cui, *Adv. Funct. Mater.* **2021**, *31*, 2100275.

[29] L. Bao, Q. Ma, R. Y. Wu, X. Fu, J. Wu, T. J. Cui, *Adv. Sci.* **2021**, *8*, 2100149.

[30] G. Zheng, N. Zhou, L. Deng, G. Li, J. Tao, Z. Li, *Opt. Express* **2021**, *29*, 2920.

[31] J. Sung, G.-Y. Lee, C. Choi, J. Hong, B. Lee, *Adv. Opt. Mater.* **2019**, *7*, 1801748.

[32] S. Chen, Y. Zhang, Z. Li, H. Cheng, J. Tian, *Adv. Opt. Mater.* **2019**, *7*, 1801477.

[33] A. Arbabi, E. Arbabi, S. M. Kamali, Y. Horie, S. Han, A. Faraon, *Nat. Commun.* **2016**, *7*, 13682.

[34] B. Groever, W. T. Chen, F. Capasso, *Nano Lett.* **2017**, *17*, 4902.

[35] D. Tang, L. Chen, J. Liu, X. Zhang, *Opt. Express* **2020**, *28*, 12209.

[36] Y. Zhou, I. I. Kravchenko, H. Wang, J. R. Nolen, G. Gu, J. Valentine, *Nano Lett.* **2018**, *18*, 7529.

[37] Y. Zhou, I. I. Kravchenko, H. Wang, H. Zheng, G. Gu, J. Valentine, *Light Sci. Appl.* **2019**, *8*, 80.

[38] M. Mansouree, H. Kwon, E. Arbabi, A. McClung, A. Faraon, A. Arbabi, *Optica* **2020**, *7*, 77.

[39] A. Arbabi, E. Arbabi, Y. Horie, S. M. Kamali, A. Faraon, *Nat. Photonics* **2017**, *11*, 415.

[40] C. Zhou, W.-B. Lee, C.-S. Park, S. Gao, D.-Y. Choi, S.-S. Lee, *Adv. Opt. Mater.* **2020**, *8*, 2000645.

[41] K. Tanaka, D. Arslan, S. Fasold, M. Steinert, J. Sautter, M. Falkner, T. Pertsch, M. Decker, I. Staude, *ACS Nano* **2020**, *14*, 15926.

[42] H. Li, W.-B. Lee, C. Zhou, D.-Y. Choi, S.-S. Lee, *Adv. Opt. Mater.* **2021**, *9*, 2100796.

[43] G. Zheng, W. Wu, Z. Li, S. Zhang, M. Q. Mehmood, P. He, S. Li, *Opt. Lett.* **2017**, *42*, 1261.

[44] L. Chen, Y. Hao, L. Zhao, R. Wu, Y. Liu, Z. Wei, N. Xu, Z. Li, H. Liu, *Opt. Express* **2021**, *29*, 9332.

[45] X. Cai, R. Tang, H. Zhou, Q. Li, S. Ma, D. Wang, T. Liu, X. Ling, W. Tan, Q. He, S. Xiao, L. Zhou, *Adv. Photonics* **2021**, *3*, 036003.

[46] D. Frese, Q. Wei, Y. Wang, L. Huang, T. Zentgraf, *Nano Lett.* **2019**, *19*, 3976.

[47] A. Arbabi, Y. Horie, M. Bagheri, A. Faraon, *Nat. Nanotechnol.* **2015**, *10*, 937.

[48] S. Gao, S.-S. Lee, E.-S. Kim, D.-Y. Choi, *Nanoscale* **2018**, *10*, 12453.

[49] R. W. Gerchberg, W. O. Saxton, *Optik* **1972**, *35*, 237.

[50] J. C. Ramirez, J. N. Schianti, M. G. Almeida, A. Pavani, R. R. Panepucci, H. E. Hernandez-Figueroa, L. H. Gabrielli, *Opt. Mater. Express* **2017**, *7*, 2651.

[51] Z. Yu, J. Hwu, Y. Liu, G. Gauzner, K. Lee, D. Kuo, *J. Appl. Phys.* **2011**, *110*, 014303.